Lab on a Chip

PAPER

View Article Online
View Journal | View Issue

Cite this: *Lab Chip*, 2022, **22**, 1989

A modular microfluidic platform to enable complex and customisable *in vitro* models for neuroscience†

D. Megarity, [a] R. Vroman, [b] M. Kriek,[c] P. Downey,[d] T. J. Bushell [e] and M. Zagnoni *[b]

Received 3rd February 2022,
Accepted 11th April 2022

DOI: 10.1039/d2lc00115b

rsc.li/loc

Disorders of the central nervous system (CNS) represent a global health challenge and an increased understanding of the CNS in both physiological and pathophysiological states is essential to tackle the problem. Modelling CNS conditions is difficult, as traditional *in vitro* models fail to recapitulate precise microenvironments and animal models of complex disease often have limited translational validity. Microfluidic and organ-on-chip technologies offer an opportunity to develop more physiologically relevant and complex *in vitro* models of the CNS. They can be developed to allow precise cellular patterning and enhanced experimental capabilities to study neuronal function and dysfunction. To improve ease-of-use of the technology and create new opportunities for novel *in vitro* studies, we introduce a modular platform consisting of multiple, individual microfluidic units that can be combined in several configurations to create bespoke culture environments. Here, we report proof-of-concept experiments creating complex *in vitro* models and performing functional analysis of neuronal activity across modular interfaces. This platform technology presents an opportunity to increase our understanding of CNS disease mechanisms and ultimately aid the development of novel therapies.

Introduction

Diseases of the central nervous system (CNS) are the second leading cause of death globally and the leading cause of disability-adjusted life years.[1] In Europe alone, they are estimated to affect 165 million people with combined direct and indirect healthcare costs of around €800 billion per year.[2,3] Furthermore, as most of the western world has an ageing population, the prevalence and associated burden of neurodegenerative diseases is set to increase substantially. The structural and functional organisation of the brain is complex and so research that leads to an increased understanding of its physiology in healthy and diseased states will be critical for the development of novel effective treatments. However, current *in vitro* models are often unable to recapitulate many aspects of the *in vivo* microenvironment, especially when considering complex neuronal circuitry and region-specific responses.[4] Furthermore, many animal models fail to recreate the critical features seen in human disease.[5] This dearth of reliable *in vitro* and *in vivo* models makes translation to the clinical setting difficult and increases the risk of late-stage failure in clinical trials.[6,7] Therefore, advanced tools for *in vitro* cell-based experiments are needed to facilitate the study of complex neuronal networks that more closely mimic brain structure and function *in vivo*.

Microfluidics, which has been used in neuroscience research for almost 20 years,[8–10] is a technology that offers several advantages over traditional cell culture techniques including the ability to spatially guide neuronal and axonal growth into ordered patterns whilst enabling the formation and investigation of synaptically connected neuronal networks.[9] The technology has been applied to a wide range of applications in neuroscience research, including the study of neurodegenerative diseases,[11,12] co-cultures with glial and other cell types,[12–15] recreation of specific networks and multi-regional modelling,[16–19] axonal insult and regeneration,[20,21] 3D culturing and modelling of the blood–brain barrier[22–25] and has been used with patient-specific iPSC-derived neuronal cultures.[26,27] Despite the tremendous

[a] *Centre for Doctoral Training in Medical Devices and Health Technologies, Department of Biomedical Engineering, University of Strathclyde, Glasgow, G4 0NW, UK*
[b] *Centre for Microsystems and Photonics, Department of Electronic and Electrical Engineering, University of Strathclyde, Glasgow, G1 1XW, UK. E-mail: michele.zagnoni@strath.ac.uk*
[c] *UCB Pharma Ltd., Slough, UK*
[d] *UCB Biopharma, Chemin du Foriest, 1420 Braine-l'Alleud, Belgium*
[e] *Strathclyde Institute of Pharmacy and Biomedical Sciences, University of Strathclyde, Glasgow, G4 0RE, UK*

† Electronic supplementary information (ESI) available. See DOI: https://doi.org/10.1039/d2lc00115b

opportunities offered, widespread uptake of microfluidics in neuroscience research has been limited by the lack of in-house microfabrication facilities and the requirement of specialist equipment, as well as limited experimental flexibility due to the fixed-layout of commercially available devices.[9,10,28] Therefore, microfluidic devices that can be easily reconfigured by assembling their components into user-defined geometries, could be suitable for a broad range of research applications and would offer a flexible solution to the design of experiments where complex cellular architecture is required. Such a platform may facilitate the uptake of microfluidic technology in many neuroscience laboratories, providing the end user with numerous possibilities to design bespoke and physiologically relevant *in vitro* neuronal cultures and enhance their research capabilities. Recently, modular microfluidic approaches have been developed using soft-lithography, 3D printing and pressure-sealing approaches.[28–35] Microfluidic assembly blocks have been moulded using SU8 (ref. 34 and 35) with integrated tongue-and-groove interlocking features,[33] whilst other examples have been directly inspired by Lego®, utilising 3D printing[29] or micromachining[30] and relying on native PDMS hydrophobicity, o-ring integration and tubing for leak-free assembly between components. However, these examples have been focussed on creating customisable chemical assays or basic cell assays, with a lack of architectures suitable for complex cell network formations between modules.

Here, we present a novel modular microfluidic platform for *in vitro* neuroscience research, composed of multiple interlocking units that interface *via* protrusions and intrusions on a pressure sensitive adhesive film. This design provides the user freedom to build customisable microfluidic devices that can be reconfigured to develop bespoke *in vitro* neuronal cultures for numerous assays within one modular system. The protocols do not require specialist equipment for platform assembly. As proof-of-concept work, we show a range of modular configurations and related applications to assess the growth and functionality of primary rat hippocampal cell cultures. Immunocytochemical staining confirmed robust neurite growth across module interfaces and shows that this can be influenced by edge-guided microchannel patterns.[36] Calcium imaging confirmed that cell cultures are functional, and that synaptic communication occurs across multiple modular interfaces. Furthermore, by utilising pre-formed fibrils of alpha synuclein to induce Lewy body-like pathology, we were able to demonstrate that our modular platform can be used to study the mechanisms which underlie the spread of pathological proteins in neurodegenerative diseases. Overall, this modular platform is a researcher-friendly tool for creating complex and customisable neuronal cultures, enabling the development of innovative cell-based assays to advance our understanding of the physiology and pathophysiology of CNS disorders.

Results

Principle of modular assembly and device configurations

The PDMS modules were designed by adapting common microfluidic features present in the literature to a modular interlocking approach based on intrusions and protrusions (Fig. 1a). The modules consist of cell culture chambers with small microchannels and an outward lip, termed protrusion (Fig. 1a-i), and one or multiple culture chambers with an inner cavity, termed intrusion (Fig. 1a-ii). By interfacing protrusion and intrusion features of different modules, several microfluidic device configurations could be obtained, enabling serial and parallel neuronal culture conditions. A width of 12 mm was arbitrarily selected for the interfacing section between protrusions and intrusions, as this provided a suitable length for the microchannel array as well as for bonding to the substrate. In laser cut acrylic moulds, the average width of a protrusion was 11.95 ± 0.01 mm (n = 10) whilst the average width of an intrusion was 11.65 ± 0.01 mm (n = 26). The module height (H) and interface height (h) were determined by the thickness of the acrylic moulds used for module fabrication (see Materials and methods). These modules, when combined, provide a lateral 'overlap', where the width of the protrusion (P) is slightly larger than the width of the intrusion (I), to enable a press-fit water-tight seal aided by PDMS–PDMS conformal bonding[29] on the PSA film (Fig. 1a-iii). The success rate in achieving leak-free interfaces when press fitting any two randomly selected modules was 66% using only ethanol solution for priming/sterilising the devices. However, it is noted that the majority of leaking interfaces did not present disruption in achieving successful cultures or perform assays. Nonetheless, to minimise this unwanted effect when using multi module large devices, a small drop of premixed PDMS was placed at either side of the interface, eliciting an overall success rate of around 90%. As proof-of-concept, four different modules were designed (Fig. 1b) to create a wide range of device configurations and subsequent assays. The combination of such modules permits the creation of bespoke devices with many culture chambers connected in series and/or parallel (Fig. 2).

The interface between modules does not present a barrier to neurite outgrowth

To assess the capabilities of the modular system in permitting cellular growth and connectivity across the protrusion-intrusion interfaces when combined with a PSA film substrate, modular 2-chamber devices were initially tested. Protocols were adapted from monolithic devices[37,38] to obtain successful cell culture and synaptic connectivity between modules. Cellular distribution was evident throughout culture chambers as confirmed with βIII-tubulin staining (Fig. 3a-i), with the presence of neurite growth between separate modules and astrocyte protrusions only seen in the entrances to microchannels (Fig. 3a-ii and iii). The interface was tested using straight channels as well as edge-guided microchannel patterns to achieve unidirectional

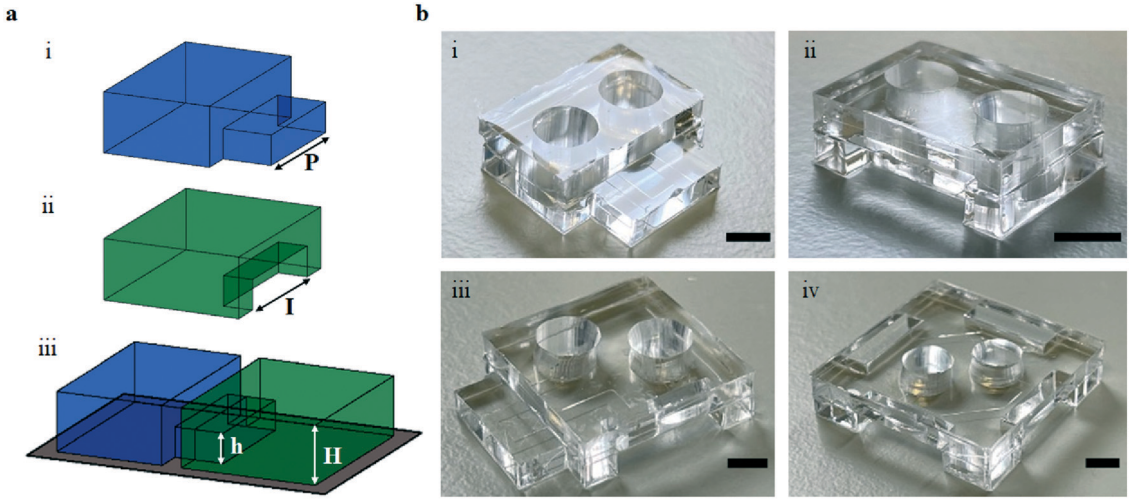

Fig. 1 The protrusion–intrusion interface is assembled by press-fitting two modules together over a pressure sensitive, biocompatible film. a Schematic of (i) a protrusion presenting module with width *P* and (ii) an intrusion presenting module with width *I*. When combined, a sealed interface is produced on the film, forming a microfluidic device for neuronal culture (iii). The protrusion/intrusion section has height *h*, while the main module body has height *H*. b Images of the four PDMS modules produced, consisting of modules with (i) one protrusion, (ii) one intrusion, (iii) one protrusion and one intrusion and (iv) four intrusions. Scale bars = 5 mm.

axonal growth across the microchannels (Fig. 3b-i–iii). For the latter, a pattern of 'heart and arrow' structures were used,[36] this encouraged forward neurite growth (Fig. 3b-iv) whilst preventing reverse neurite outgrowth (Fig. 3b-v) after 14 DIV (Fig. S1†). Subsequently to this, functionality of neuronal cultures grown across the modular interface was tested.

Functional synaptic connectivity is observed between individual modules

Ca^{2+} imaging protocols previously developed for probing functional synaptic connectivity between fluidically isolated neuronal populations were adapted for modular 2-chamber devices (Fig. 4a).[37,38] Here, we show that

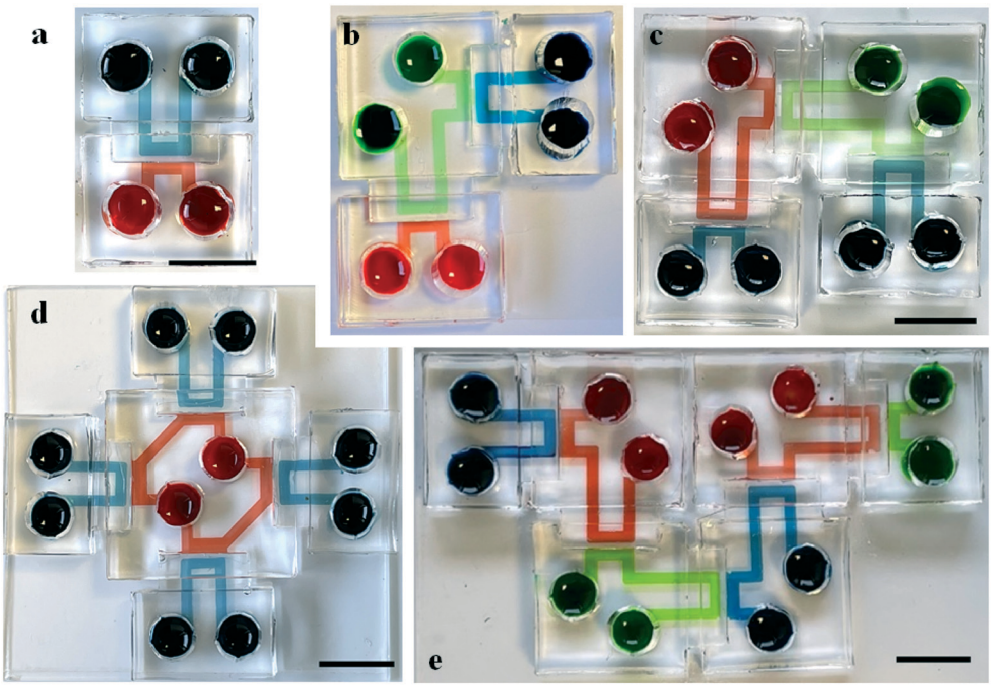

Fig. 2 A range of multi-module devices with series or parallel culture configurations can be obtained by combining the individual PDMS units. Examples of device configurations where different coloured solutions highlight the culture chambers in each module. a A two-module device. b A three-module device. c A four-module device connected in series. d A five-module device with four modules independently connected to a central module, demonstrating parallel connectivity. e A six-module device connected in series. Scale bars = 10 mm.

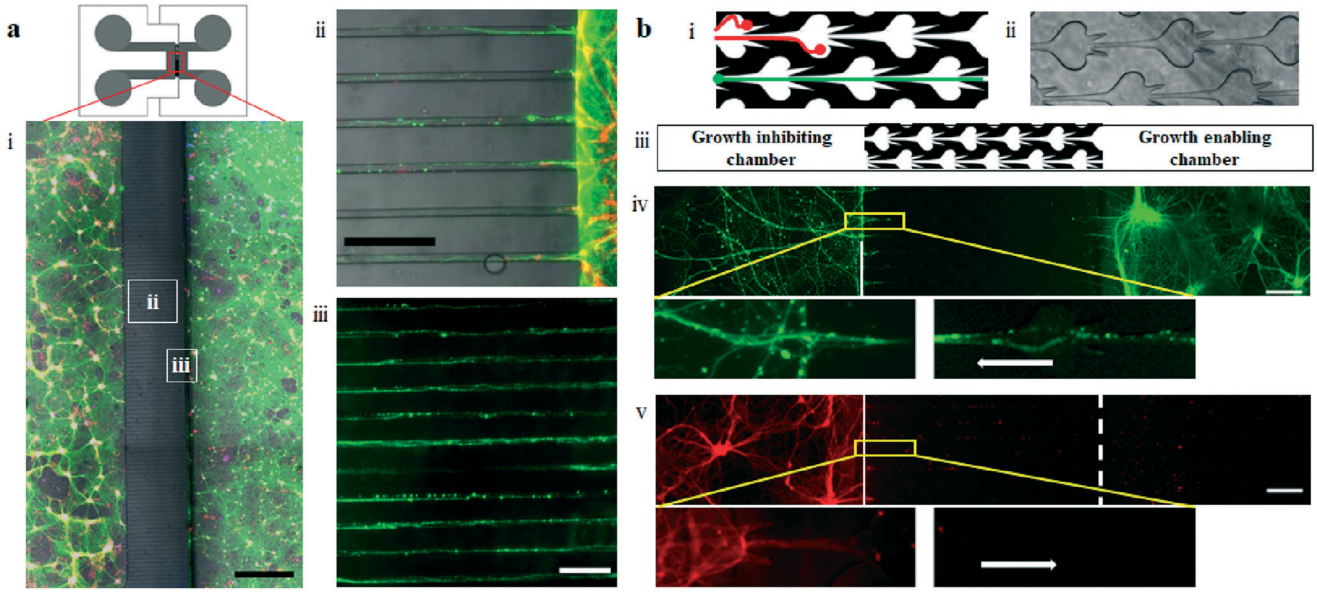

Fig. 3 Immunocytochemical staining confirms neurite growth of primary rat hippocampal cells cultured across a protrusion–intrusion interface in 2-chamber modular devices. a Cellular distribution is evident throughout culture chambers (i) of both a protrusion (left) and an intrusion (right) module after 14 DIV, with (ii) neurites able to cross the modular interface and (iii) grow throughout microchannels. Green = βIII-tubulin, red = GFAP. Scale bars = (i) 500 μm and (ii and iii) 100 μm. b Modular two-chamber device containing 'heart-arrow' edge-guided microchannels to direct neurite growth. (i) Heart-arrow microstructures enabling permissive (green) and inhibitive (red) edge guidance of neurites and (ii) representative brightfield image of PDMS microchannels. (iii) Device schematic of edge-guidance, with (iv) permissive growth in the forward orientation (green) and (v) inhibiting growth in the reverse orientation (red). Inserts show neurite presence or absence in microchannels. Red and green = βIII-tubulin. White dashed line indicates the modular interface and edge of microchannel region. Solid white line indicates edge of adjacent culture chamber. Scale bars = 200 μm.

hippocampal cultures are healthy and synaptically connected between chambers, as demonstrated by an increase in calcium responses from neurons after direct and indirect chemical stimulation (Fig. 4b and c). Fluidic isolation between all chambers was maintained using appropriate hydrostatic pressure conditions (Fig. S2,† for validation of protocol) and cellular activity monitored over a period of 3 minutes, with G added at t = 1 minute, followed by KCl at t = 2 minutes (Fig. 4a and b) (Movie S1 in ESI†).

First, glutamate (G, 100 μM) was added to one culture chamber (chamber highlighted in blue in Fig. 4a), resulting in an increase in the number of Ca^{2+} events from 0 events/s to $18.28 \times 10^{-3} \pm 0.21 \times 10^{-3}$ events/s ($p < 0.0001$, baseline *vs.* G, n = 62 cells in 3 devices from 3 separate cultures). An increase in Ca^{2+} events was also observed in the indirectly stimulated but synaptically connected adjacent neurons, from 0 events/s to $8.31 \times 10^{-3} \pm 0.61 \times 10^{-3}$ events/s ($p < 0.0001$, baseline *vs.* G, n = 203 cells in 3 devices from 3 separate cultures) (chamber highlighted in black in Fig. 4a). To further assess functionality, KCl (30 mM) was subsequently added to the previously indirectly stimulated side (chamber highlighted in black Fig. 4a), where an increase in Ca^{2+} events from 0 events/s to $17.35 \times 10^{-3} \pm 0.20 \times 10^{-3}$ events/s ($p < 0.0001$, baseline *vs.* KCl) was obtained. This also elicited an increase from 0 events/s to $23.92 \times 10^{-3} \pm 1.25 \times 10^{-3}$ events/s ($p < 0.0001$, baseline *vs.* KCl) in the opposite culture chamber, showing bidirectional synaptic communication in hippocampal cultures.

Neuronal networks grown across modular interfaces are amenable for *in vitro* studies of neurodegeneration

To show proof of concept regarding suitability of the platform for studying mechanisms of neurodegeneration, a 3-module device was used where one chamber (highlighted in red in Fig. 4d-i) was seeded with α-synuclein pre-formed fibrils (PFFs) to induce the formation of cellular aggregates which can be detected by the appearance of phosphorylation of α-synuclein at serine-129 (pSer-129-αSyn), a disease-specific biomarker used to detect Lewy bodies in Parkinson's disease[39] (Fig. 4d). In the target chamber (red/chamber 1, Fig. 4d-i), the PFFs produced pSer-129-αSyn, evident by the typical punctate and thread-like pSer129 staining (Fig. 4d-ii), used as an unbiased measure of molecular pathology.[40,41] pSer-129 staining was also evident in the adjacent synaptically connected but fluidically isolated chamber 2 (Fig. 4d-iii), with a reduced level of 0.12% ± 0.01% compared with 0.46% ± 0.08% in the target chamber (p = 0.03) and no punctate or thread-like staining observed in chamber 3. This reduction in pSer-129-αSyn staining in non-target chambers is indicative of spread of pathological alpha-synuclein across modules. To prevent passive transport of PFF solution between the target and adjacent chambers, a hydrostatic pressure gradient towards

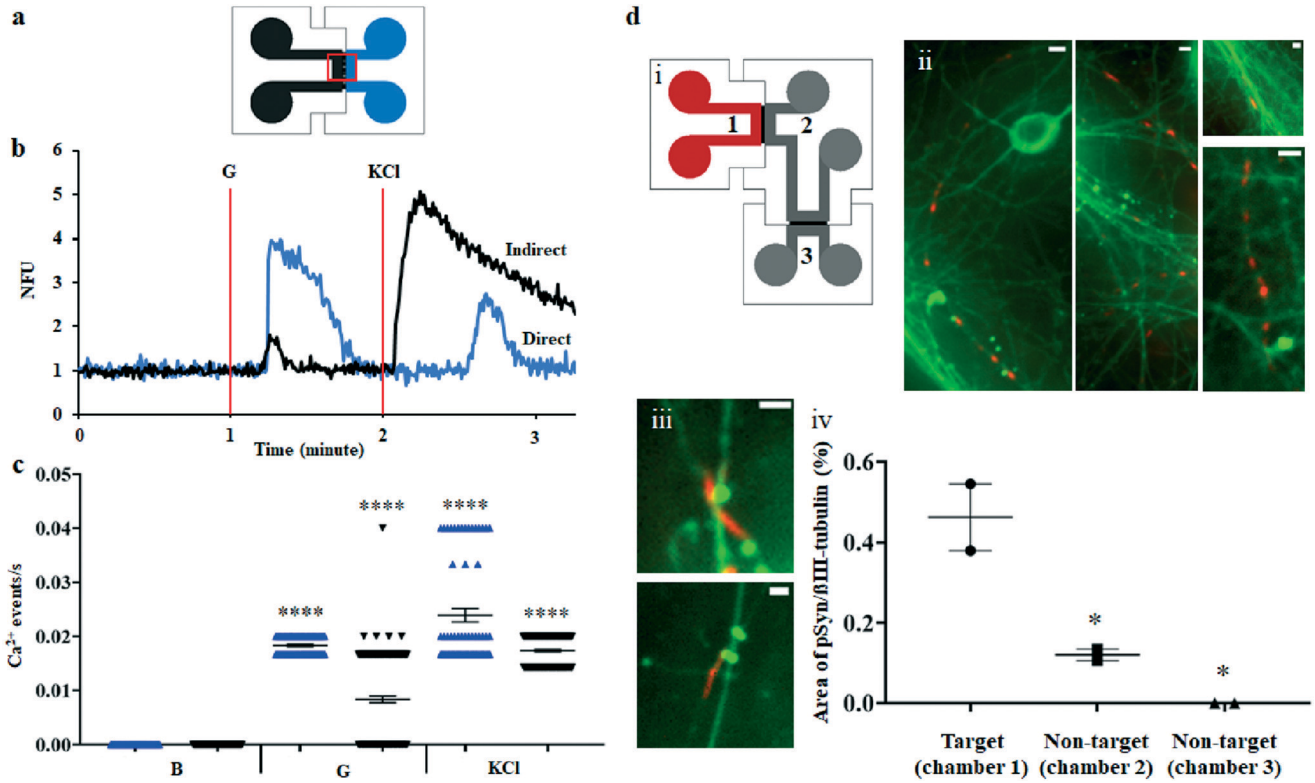

Fig. 4 Immunocytochemical staining and calcium imaging confirms primary rat hippocampal cells grown across a protrusion–intrusion interface are synaptically connected and amenable to neurodegenerative *in vitro* studies. Ca^{2+} imaging (10–12 DIV) revealed functional connectivity between fluidically isolated cell populations, suggesting primary hippocampal cultures are healthy and the modular interface does not create a barrier to functional synaptic connectivity. a Schematic of a 2-module device, with culture chambers connected by linear microchannels. b Representative fluorescence intensity traces of Ca^{2+} response for a single neuron in the direct (blue) and indirect (black) chambers, where glutamate was applied to the blue chamber only and KCl to the black chamber only. NFU = normalised fluorescence units. c The number of Ca^{2+} events increases in both chambers in response to direct and indirect chemical stimulus. Chart shows mean ± S.E.M., n = 62 cells in direct side and 203 cells in indirect side of 3 devices from 3 separate cultures. A one-way ANOVA with Tukey's multiple comparison's test was used to compare events/s. **** = $p <$ 0.0001 *vs.* baseline. d Modular devices can be used as tools for investigating neurodegenerative disease mechanisms. (i) Schematic of a 3-module device where PFFs were added to chamber 1 (red module) after 7 DIV, with cells fixed and stained after 14 DIV. (ii) pSer129 staining indicates internalisation and phosphorylation of α-synuclein fibrils, evident by both punctate and thread-like features (red) and (iii) subsequent appearance of phosphorylated α-synuclein to a fluidically isolated but synaptically connected adjacent neuronal population. Scale bars = 5 μm. (iv) The level of pSyn in each chamber of 3-module device (d), was calculated as a percentage of the level of βIII-tubulin, demonstrating a reduction in the non-target chamber 2, whilst no pathological-like staining was observed in chamber 3 (n = 2 images from each chamber of 1 device).

the target chamber was created following established protocols (Fig. S2†).

Functional connectivity is observed across multiple modular interfaces

To probe functional synaptic connectivity across multiple modules, modular 3-chamber devices were examined. βIII-tubulin revealed uniform neuronal distribution throughout the culture chambers in the three modules (Fig. 5a). Ca^{2+} imaging experiments were designed to assess neuronal functionality across multiple modules. Cells in chamber 1 (red) were directly stimulated using 0 Mg^{2+}, which has been previously shown to enhance neural activity over extended periods of time,[42–44] resulting in Ca^{2+} responses recorded in chamber 2 (green) and chamber 3 (blue), (Fig. 5b). Fluidic isolation between all chambers was maintained using appropriate hydrostatic pressure conditions and cellular activity monitored over a period of 30 minutes at regular intervals (Fig. S2†).

Approximately 20 minutes after the addition of 0 Mg^{2+} HBS to chamber 1, an increase in activity was observed in both the indirectly stimulated cell populations (chambers 2 and 3) with respect to unstimulated cases. In chamber 2, there was an increase in Ca^{2+} events from 0 events/s over the baseline period (t = 0–2 minutes) to $0.74 \times 10^{-3} \pm 0.16 \times 10^{-3}$ events/s over the post-incubation period (t = 20–30 minutes) ($p < 0.0001$, baseline *vs.* post-incubation, n = 64 cells from 2 separate devices from 2 separate cultures), and in chamber 3 this increased from 0 events/s to $0.72 \times 10^{-3} \pm 0.16 \times 10^{-3}$ events/s (p = 0.0001, baseline *vs.* post-incubation, n = 57 cells from 2 devices from 2 separate cultures) (Fig. 5d, left). In control experiments, the addition of normal HBS solution to chamber 1 in place of the 0 Mg^{2+} HBS did not elicit a significant increase in neuronal events (Fig. 5d, right). These results suggest the spontaneous generation of activity in

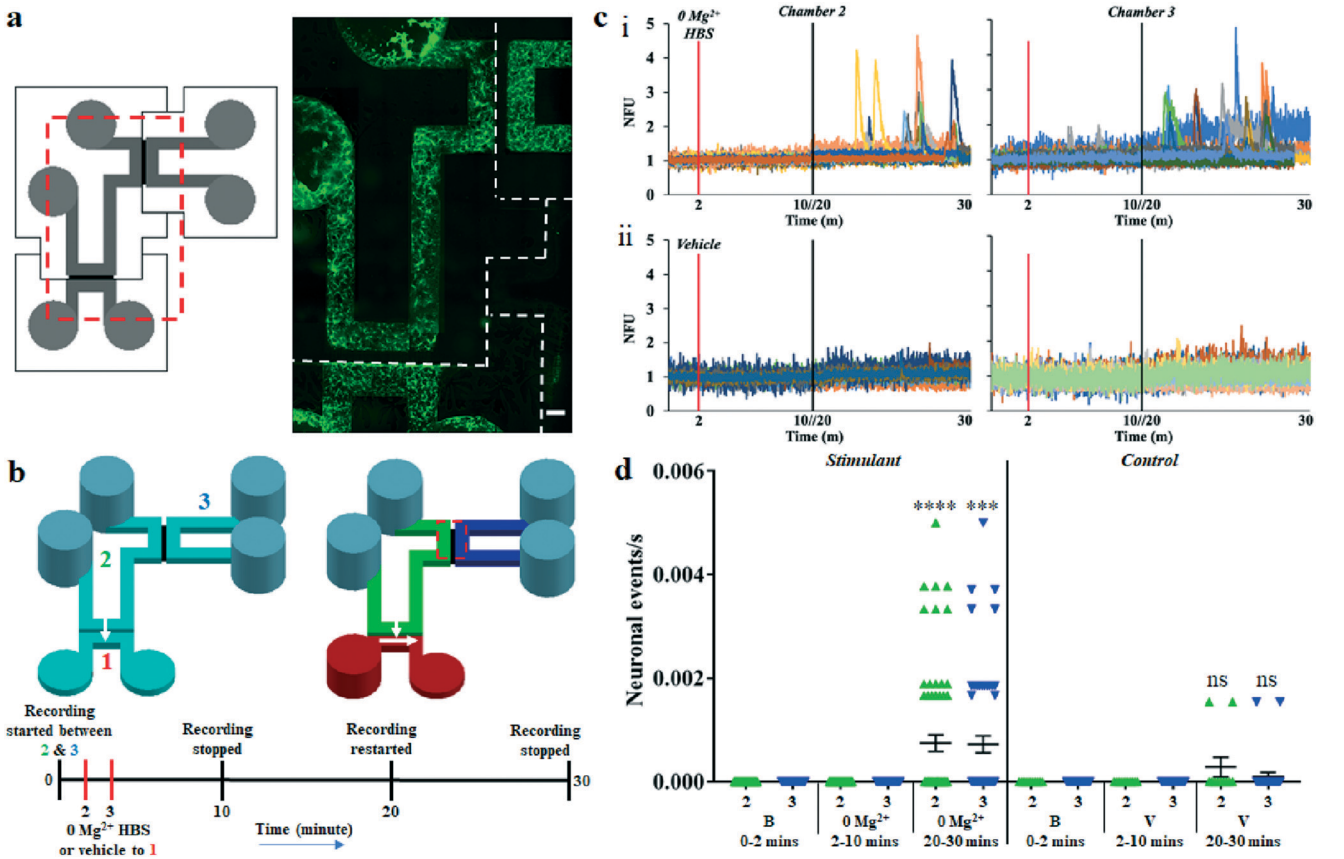

Fig. 5 Functional synaptic connectivity is observed across multiple modular interfaces. a A 3-module device seeded with primary hippocampal cultures indicating uniform neuronal cell distribution, evident by βIII-tubulin staining (green). White dashed lines indicate outline of individual modules. Scale bar = 1 mm. b Timeline and schematic of Ca^{2+} imaging experiment in 3-module devices with 0 Mg^{2+} HBS solution (stimulant) used to increase neuronal activity. The stimulant was added to chamber 1 (red), with recording between chambers 2 (green) and 3 (blue) (red dashed box). c Fluorescence intensity traces of neuronal Ca^{2+} response in chambers 2 (left) and 3 (right) following addition of either (i) 0 Mg^{2+} HBS or (ii) normal Mg^{2+} HBS (vehicle solution), with an increase in activity observed following the addition of 0 Mg^{2+} HBS, compared to control. NFU = normalised fluorescence units. d Increase in neuronal Ca^{2+} events from the baseline period (t = 0–2 minutes) to the period following incubation with the stimulant (t = 20–30 minutes) in both chambers 2 and 3. Scatter chart shows mean ± S.E.M., n = 64 responsive neurons in chamber 2 and 57 responsive neurons in chamber 3 from 2 separate devices/cultures loaded with stimulant and 12 responsive neurons in chamber 2 and 30 responsive neurons in chamber 3 from 1 device/culture loaded with the control. *B* = baseline, *V* = vehicle. A one-way ANOVA was used to compare events in each chamber over the baseline period (t = 0–2 min), the period following 0 Mg^{2+}/V addition (t = 2–8 min) and the post-incubation period (t = 20–30 min). *** = $p < 0.001$ and **** = $p < 0.0001$ *vs.* baseline. ns = non-significant ($p > 0.05$).

chambers 2 and 3 is due to functional connectivity with cells in chamber 1 following the 0 Mg^{2+} HBS incubation period (Movie S2†).

Multi-modular devices allow the formation of complex interconnected cultures for novel assays

To further demonstrate the potential of our modular platform, we produced devices with complex geometries comprised of multiple modules (Fig. 6). These included a 4-chamber device with all chambers interconnected in series (Fig. 6a), a 5-chamber device using the central intrusion module to highlight parallel connectivity (Fig. 6b) and a 6-chamber device to show a more complex device with cultures connected in series (Fig. 6c). The maximum number of modules used in the present study was six due to the dimensions of the glass slides used for improving the stability of the assembled devices. However, more modules could be used as required using larger glass slides. These more complex configurations showed cellular distribution throughout culture chambers with neurites entering microchannels and transecting the modular interface.

Discussion

Here, we show proof-of-concept work using a modular microfluidic platform which enables the production of complex, user-defined cellular culture patterns. The platform comprises multiple microfluidic PDMS modules that interface *via* a simple protrusion–intrusion, self-sealing mechanism on a pressure sensitive adhesive film substrate. We demonstrate, using primary hippocampal cultures, that functional synaptic connectivity is maintained across the modular interface and show a range of device configurations

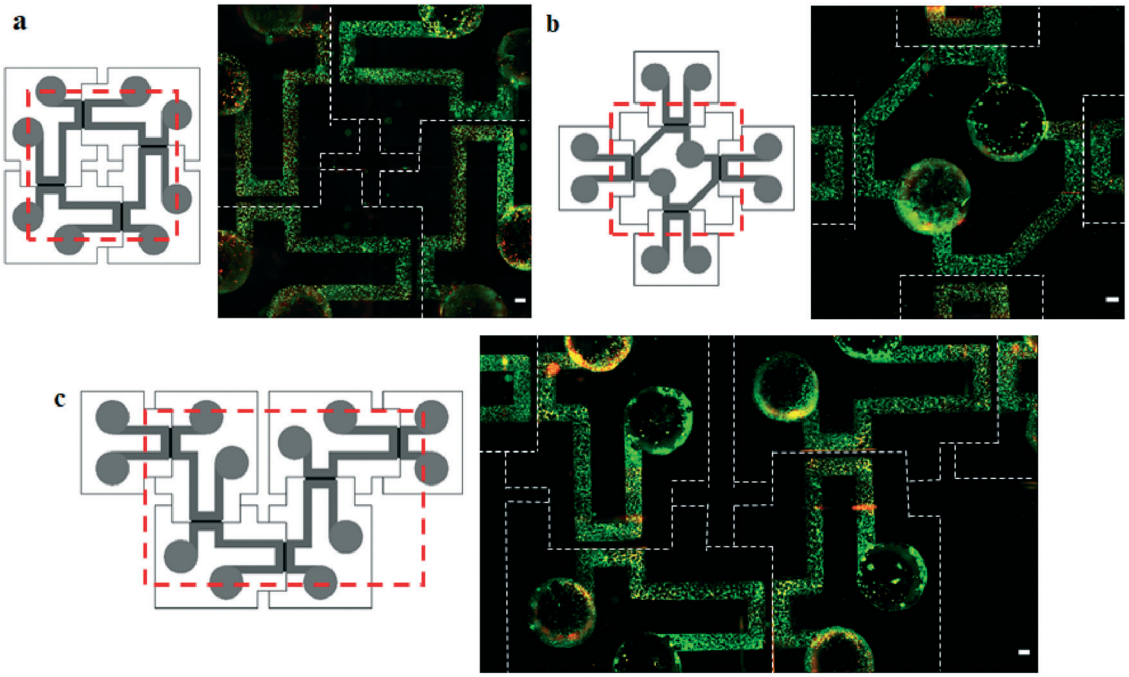

Fig. 6 The modular system enables the production of complex *in vitro* neuronal cultures and customisable assays. a A 4-module device with all modules interconnected in a loop. b A 5-module device with four modules independently connected to a central module, highlighting parallel connectivity. c A 6-module device with all modules connected in series. Green = βIII-tubulin, red = GFAP, cultures fixed and stained after 14 DIV. Red dashed lines indicate location of imaging and white dashed lines indicate the outlines of individual modules. Scale bars = 1 mm.

to suggest potential applications. Our proposed modular system offers unrivalled flexibility for the development of a vast array of user-specified assays to enable novel *in vitro* neuroscience research, which is simply not possible with traditional monolithic device equivalents. Given the specific challenges in brain disorders, drug discovery and the translational issues with animal models, improved *in vitro* models are likely to play a pivotal role by recapitulating specific circuitry and microenvironmental conditions.

The use of adhesive tapes for assembling devices enables cost-effective and simple assembly, while the specific use of pressure sensitive adhesive films provide bond strengths similar to plasma bonding.[45] Additionally, the use of a non-permanent bonding mechanism enables disassembly of PDMS modules and their subsequent reuse, enabling greater flexibility. The four modules we have designed provide the ability to create complex culture networks to recapitulate specific circuitry as seen *in vivo*, permitting the assembly of multiple chambers connected in series (using sequential protrusion-intrusion modules) or in parallel (using the central all-intrusion module). The arbitrary interface dimensions used in this work enable practical integration of microfluidic components and their self-sealing. The laser cutting tools used to produce the acrylic moulds generated typically smooth surfaces for casting PDMS, but sometimes produced irregular features in the vertical walls of the resulting PDMS modules (due to defects produced by localised melting of the acrylic), culminating in weak seals at the interface. Characterisation of any two modules combined showed a success rate of 66% using ethanol priming to achieve leak-free interfaces. Therefore, as a provisional measure, premixed liquid PDMS was applied at the interfaces to decrease leakage occurrence when using multi-module devices. Further investigation into alternative fabrication methods for the moulds and module material (including hard plastic) is required to produce defect-free modules, ensuring consistent hermitic sealing and provide scalability of the modules for mass production. This could include the use of 3D printing, thick film SU8 resists for creating moulds[46–48] as well as alternative soft lithography materials.[49,50]

Typical microfluidic device preparation involves the use of oxygen plasma treatment to render surfaces hydrophilic and also sterile.[51,52] However, this presents a barrier to microfluidic use in neuroscience laboratories where such equipment is typically not available. To solve this, we have developed protocols using a 70% ethanol solution for priming microchannels to improve wettability and sterilising devices, an alternative procedure available to all laboratories, and compared this to oxygen plasma treated devices. Whilst the majority of cultures were successful using 70% ethanol, the occurrence of air bubbles was more frequent than with oxygen plasma. Therefore, further protocol optimisation is required to prevent bubble formation in channels and improve hydrophilicity of PDMS in solvent-sterilised devices. Regarding the coating procedure with adhesion molecules (*e.g.* poly-L-lysine), similar results to oxygen plasma treated devices were achieved using ethanol–water solutions when incubations were performed overnight, obtaining improved

culture conditions with uniform cellular distribution throughout culture chambers.

As proof-of-concept work, we have shown configurations using a maximum of six chamber devices to demonstrate complex neuronal cultures and examples of series and parallel chamber connections. However, the protrusion–intrusion modular interfacing system would enable extended designs, providing a high degree of flexibility for multi-module connectivity. We acknowledge that for this, the development of a substrate that would support a higher number of modules is required, or potentially developing smaller modules with a footprint similar to those used for well plate assays to guarantee interfacing with existing imaging equipment.

Uniform cellular growth and distribution was evident throughout all culture chambers. Whilst this has previously only been demonstrated in monolithic microfluidic devices,[8,38,53] these results show that our modular interface design does not present a barrier to neurite outgrowth between separate device modules. This highlights the possibility for creating large, interconnected networks with a greater degree of flexibility and control over regional manipulation, beyond that of the traditional monolithic devices currently available. Further, the integration of edge-guiding microstructures in the modules demonstrates the ability to use this platform to create defined *in vitro* networks and establishment of specific circuitry seen *in vivo*, with either permissive or prohibitive neurite growth depending on their orientation. Whilst we arbitrarily used a pattern of hearts and arrows in this study for demonstrating proof-of-concept directionality, other structures can equally be implemented.[17,54,55] The use of pre-formed fibrils to induce α-synuclein pathology has been well documented for its ability to study misfolding and aggregation in cultures with normal levels of endogenous α-synuclein.[41,56–58] Here, we have demonstrated the induction of α-synuclein pathology and subsequent spread of pathology across the modular interface between fluidically isolated but synaptically connected neurons. This shows that the functionality obtained by this modular system is equivalent to that of monolithic devices, but can enable the pathological spread *via* synaptic connectivity to be examined in more complex networks.

Ca^{2+} imaging confirmed healthy primary hippocampal cell growth on the PSA substrate and functional connectivity across the modular interface between separate modules (Fig. 4). The use of a 0 Mg^{2+} solution increases spontaneous neuronal activity over an extended period of time,[44] thus creating a favourable condition to observe responses to indirect stimulation in downstream modules, as opposed to just the one large response seen when using glutamate as a stimulant[38] (Fig. S4†). The 0 Mg^{2+} induced spiking activity enabled downstream observation of secondary cellular responses in the central intrusion-protrusion chamber and subsequently tertiary responses seen in the protrusion chamber (Fig. 5). The increased activity observed in both indirectly stimulated chambers in fluidic isolation is indicative of functional synaptic connectivity across the three modules, as this was absent in the control.

The main attraction of this platform is the ability to produce bespoke devices and assays within one researcher-friendly system that does not require microfabrication facilities. These characteristics present a significant step forward for researchers to design devices suitable to their needs and ultimately contribute to a greater understanding of brain circuitry and its alteration in CNS disorders. Ultimately, organ-on-chip systems that provide enhanced experimental capabilities will contribute to a reduction in animal use and speed up the drug development process through the improved predictably of response and relevance to human physiology. Future opportunities include the development of other modules that can provide further features, such as 3D culture and the development of structures including the blood–brain barrier[22,23,59] using non-neuronal cell types. Despite our focus on neuroscience applications, this modular platform would also offer a major step forward in developing body-on-chip systems, as reviewed elsewhere.[60] In this case, a modular platform would provide the ability to combine multiple components, each with a separate cell type, interconnected to recapitulate the *in vivo* organisation.

Materials and methods

Module fabrication and preparation

Microfluidic devices were fabricated in polydimethylsiloxane (PDMS) using standard soft- and photo-lithography techniques, as previously described.[37,38] Briefly, silicon masters with microfluidic features were produced through a two-layer microfabrication process depositing photoresist (SU8) on its surface. The first layer (SU8 3010) formed microchannels for connecting the culture chambers with a thickness of 14 μm (10 μm wide and aiming for a length of 500 μm between chambers), while the second layer (SU8 3035) formed the main culture chambers with a thickness of 100 μm (1500 μm wide and length dependent on modules, see Table S1†). The silicon masters were then silanised by vapour deposition of 1*H*,1*H*,2*H*,2*H*-perfluorooctyl-trichlorosilane (Sigma Aldrich, UK) for 1 hour.

To produce modular devices, two laser-cut acrylic sheets (3 mm thick) were used to mould 3-dimensional (3D) interlocking protrusions and intrusions (Fig. 1). Laser cutting was carried out using a VLS 6.60 (Universal Laser Systems, AZ, USA) using standard parameters as set in the dedicated software (60 W, 100% power and 8% speed). Dimensions for the acrylic sheets were set at 12 mm for intrusions and 11.7 mm for protrusions in drawing files. The first sheet was clamped to the silicon master wafer to create the protrusion/intrusion layout (Fig. S2†). PDMS was mixed at a 10 : 1 ratio (base to curing agent) and poured into the mould cut-outs. This was degassed for 15 minutes and cured in an oven at 80 °C for 30 minutes, while excess PDMS was left to fully degas. After curing, the first layer of PDMS was left to cool and the

clamps were removed. The second acrylic sheet was then aligned and clamped onto the first sheet, with degassed PDMS poured to create the top layer of the module and cured at 80 °C for 3 hours. After cooling, clamps were removed, and the moulds peeled from the wafer. PDMS modules were removed from the moulds and eventual excess PDMS (caused by defects in the acrylic moulds) was trimmed using a sharp scalpel or blade, with open wells created using a biopsy punch. All devices were cleaned and rinsed with isopropyl alcohol (IPA) and de-ionised (DI) water prior to assembly.

Device assembly

Modules were bonded reversibly to a single sided pressure sensitive adhesive (PSA) film, Excel Scientific ThermalSeal® RTS (Sigma Aldrich, UK) to create enclosed microfluidic devices.[45] The PSA film was cut to size and the backing film removed. Individual modules were placed sequentially on the PSA film, according to the desired device configuration, and pressure applied by gently pushing down each module. To improve the structural stability and to facilitate microscopic imaging of devices with multiple modules, a glass substrate, such as a glass coverslip or microscope slide, was attached to the PSA film using a double-sided adhesive film (3M 96042, FindTape, USA). A small amount of PDMS was deposited around the interface between modules and left to cure (RT, 24 hours) to improve hermetic sealing when using large devices. All devices were visually inspected for undesired features (channel blockage or failed bonding) under an inverted microscope prior to use.

Preparation for cell culture

Assembled devices were primed either with a solution of 70% ethanol or with oxygen plasma (Pico A Plasma Asher, Diener Electric, Germany) to test and compare wettability of the PDMS surfaces and achieve sterile conditions. Subsequently, sterile poly-L-lysine (PLL, 10 μg ml^{-1}, 1 h) or poly-L-ornithine (PLO, 100 μg ml^{-1}, 3 h) was added to each open well to coat the channels, thus aiding cell attachment. Channels were then rinsed 3× with sterile supplemented Neurobasal-A medium (2 mM L-glutamine and 2% v/v B27 with 50 U ml^{-1} penicillin and 50 μg ml^{-1} streptomycin). Devices were then stored in a humidified incubator prior to cell culture.

Primary hippocampal cell culture

Cell culture was performed as previously described.[37,38] Briefly, Sprague Dawley rat pups (1–3 days old) were killed *via* cervical dislocation, in accordance with schedule 1 of the Animals (Scientific Procedures) Act 1986, the brain rapidly removed, and the hippocampus dissected out. The hippocampi were chopped into small pieces and incubated in papain solution (1.5 mg ml^{-1}, 20 minutes) followed by gentle trituration in bovine serum albumin solution (BSA, 10 mg ml^{-1}). Papain and BSA were made in an enzyme solution consisting of, in mM: 116 NaCl, 5.39 KCl, 26 $NaHCO_3$, 1.3 NaH_2PO_4, 1.02 $MgSO_4$, 0.5 EDTA, 25 glucose, 1.98 $CaCl_2$. Cells were counted using a haemocytometer then resuspended in Neurobasal-A culture medium supplemented with L-glutamine (2 mM) and B27 (2% v/v) at a density of 3–5 × 10^6 cells per ml. Penicillin–streptomycin (50 U ml^{-1} penicillin, 50 μg ml^{-1} streptomycin) was added to the medium for rinsing and seeding. Cells were pipetted into the device chambers *via* open wells and incubated for 10–15 minutes prior to filling each well with culture media. The volume of cell suspension used varied by module: 9 μl added to an intrusion module, 17 μl added to a protrusion module, 30 μl added to a combined protrusion-intrusion module and 42 μl total added to an all-intrusion module (see Table S1†). 24 hours after seeding, the medium was completely replaced with antibiotic free culture media. Devices remained in a humidified incubator for 10–14 days *in vitro* (DIV) prior to experimentation, with media replenished every 2–3 days by exchanging half the well volume.

Preparation of synuclein pre-formed fibrils

Native sequence human alpha-synuclein was expressed in Expi293F cells. The protein was recovered from the culture media *via* anion exchange using a HiTrap Q column (GE Healthcare). The column was washed with 20 mM Tris/HCl pH 8.0, and protein eluted using a sodium chloride gradient to 400 mM. Fractions were concentrated and desalted by passing over a HiPrep 26/10 column (GE Healthcare) and eluted with 20 mM Tris/HCl pH 8.0. The protein was further purified using a MonoQ 10/100 GL column, eluted with a sodium chloride gradient to 400 mM in 20 mM Tris/HCl pH 8.0, followed by gel filtration on a HiLoad 26/600 Superdex 75 column (GE Healthcare), with elution in PBS pH 7.4.[40]

Alpha-synuclein fibrils were obtained by agitating purified, recombinant alpha-synuclein monomer (9–10 mg mL^{-1} in PBS pH 7.4) at 1200 rpm, 37 °C in a Vortemp 56 shaking incubator (Labnet), shaking continuously for 10 days. Fibril formation was assessed by JC-1 assay[61] and Fourier transform infrared spectroscopy of the solution. Unincorporated monomer in the fibril solutions was assessed by ultracentrifugation and by passage through a 100 KDa cut-off membrane followed by gel electrophoresis. The prepared fibrils were stored at −80 °C.

α-Synuclein pre-formed fibril seeding

Hippocampal cultures were prepared as before, with α-synuclein pre-formed fibrils (PFFs)[40] added after 7 DIV. Prior to their addition (final concentration 1 μg ml^{-1}), PFF aliquots were wrapped in parafilm and sonicated in a water bath to reduce fibril size and improve seeding (35 °C, 37 kHz, 25 minutes – ~5 minutes on, 1 minute off and repeat). Hydrostatic pressure gradients were induced, by appropriately altering well volumes, to prevent flow of PFFs from target chambers to adjacent chambers (see Fig. S2†). PFFs were added to one open well of the target chambers and incubated for 15 minutes. This was repeated by adding PFFs to the opposite open well of the same chamber, and

once again into the initial well. Finally, PFF solution was washed, and fresh media added to all wells creating a flow gradient across the microchannels to prevent possible contamination and diffusion of PFFs into the non-target chambers. Cultures were incubated for a further 7 days. Media was refreshed by ensuring the volumes in the target chambers always remained lower than in the adjacent chambers. Immunocytochemical staining was performed on cultures after 14 DIV. To quantify the level of pSer-129-α-syn in target and non-target chambers, fluorescent images were converted to binary in ImageJ, and the areas of pSer-129-α-syn and βIII-tubulin staining calculated. The level of pSer-129-α-syn was then presented with the area of pSer-129-α-syn as a percentage of the area of βIII-tubulin.

Immunocytochemistry

Immunocytochemical staining was performed on cultures as previously described.[37,38] Cells were washed with phosphate buffered saline (PBS) and fixed with ice-cold paraformaldehyde (4%) for 10 minutes. Cells were then permeabilised using Triton-X 100 (0.1% in PBS) applied for 10 minutes. Washed with PBS and incubated with a blocking solution containing foetal bovine serum (FBS, 5% v/v) and BSA (1% w/v) in PBS for 1 hour at room temperature. Primary antibodies were diluted in blocking solution (1 : 500) and incubated with the cultures at 4 °C overnight. Antibodies used were rabbit anti-βIII-tubulin (T2200, Sigma-Aldrich, UK; neuronal marker), mouse anti-synaptophysin (AB8049, Abcam, UK; synaptic vesicle marker) and chicken anti-GFAP (AB5541, Sigma-Aldrich, UK; glial fibrillary acidic protein, marker for astrocytes). For PFF experiments, rabbit anti-α-synuclein (phosphorylated serine 129; AB51253, Abcam, UK; 1 : 300 in blocking solution) primary antibody was used for its robustness at specifically targeting phosphorylated and not wild-type α-synuclein,[62] alongside mouse anti-βIII-tubulin (AB78078, Abcam, UK; 1 : 500 in blocking solution) were used. Cells were then rinsed with PBS and incubated with the relevant fluorescently labelled secondary antibodies, all diluted 1 : 200 in blocking solution, for 1 hour at room temperature (anti-rabbit or anti-mouse Alexa Fluor 488; anti-rabbit or anti-mouse Alexa Fluor 555; and anti-chicken Alexa Fluor 633; all from ThermoFisher, UK). Finally, cells were rinsed 3× with PBS and wells filled with PBS prior to imaging on an inverted microscope (AxioObserver 7, Zeiss, Germany), with images taken using an ORCA-Flash 4 camera (Hamamatsu, Japan).

Calcium imaging

Calcium (Ca^{2+}) imaging was performed as previously described[37,38] to determine synaptic connectivity between fluidically isolated neuronal populations in 2-module and 3-module device configurations. All devices used had straight microchannels between modules which enables bidirectional neurite connectivity. Cells were rinsed in a HEPES-based solution (HBS) consisting of (in mM): 140 NaCl, 2.5 KCl, 2 $MgCl_2$, 10 HEPES, 10 D-glucose, 2 $CaCl_2$. The pH was adjusted to 7.4 ± 0.02 using NaOH, and the osmolarity adjusted to 310 ± 2 mOsm using sucrose when required. Cells were loaded with Fluo-8 AM (4 μM in HBS) for 1 hour at room temperature and rinsed 3× with HBS prior to imaging. All experiments were performed in HBS by creating hydrostatic pressure gradients across the different modules by appropriately controlling fluid volumes in the open wells (Fig. S2†).

In 2-chamber devices, L-glutamate (G, final concentration, 100 μM) was added to induce cell depolarisation in one chamber (direct side) whilst monitoring calcium responses in both chambers, followed by addition of KCl (final 30 mM) to the opposite chamber. In 3-chamber devices, a zero-magnesium HBS solution (0 Mg^{2+} HBS) was added in one chamber (direct side) to induce neuronal bursting activity[42–44] and spontaneous Ca^{2+} responses monitored in the two adjacent indirect chambers. At the end of experiments, KCl (final concentration, 30 mM) was added to confirm neuronal viability and allow distinction between neuronal and non-neuronal signals. Images were obtained using an inverted microscope (AxioObserver 5, Zeiss) and EMCCD camera (LucaR, Andor Technology, NI) with a frame rate of 2 Hz and exposure time of 0.2 s (Andor SOLIS). A 5× objective was used for a field of view encompassing the central microchannels with a portion of culture chambers on either side. Recordings were saved as a TIFF. Regions of interest (ROI), corresponding to cell somas, were highlighted in Fiji (ImageJ) and raw data exported to Excel for manual analysis. Ca^{2+} events were considered as an increase of 0.5 NFU above the preceding or background intensity over each period of observation. These were then counted for each cell and presented as the number of events/cell per s during that period of observation.

Statistics

All data are expressed as mean ± standard error of the mean (S.E.M.), with Minitab Express or GraphPad Prism used to perform statistical analysis. One-way ANOVA with Tukey's *post hoc* test or unpaired student's *t*-test were used, with $p < 0.05$ taken as significant in all cases.

Open access

For the purpose of open access, the authors have applied a Creative Commons Attribution (CC BY) licence to any Author Accepted Manuscript version arising from this submission.

Author contributions

D. M. performed and analysed all experiments. D. M., T. J. B. and M. Z. contributed to experimental design and interpretation of results. M. K. produced PFFs. R. V. contributed to PFF experimentation and analysis. D. M., T. J. B., P. D. and M. Z. contributed to writing and editing of the manuscript.

Conflicts of interest

No competing interests to declare.

Acknowledgements

This project was supported by funding from EPSRC (grant number EP/LO15595/1) through the CDT in Medical Devices and Health Technologies at the University of Strathclyde.

References

1 V. L. Feigin, *et al.*, *Lancet Neurol.*, 2019, **18**, 459–480.
2 M. DiLuca and J. Olesen, *Neuron*, 2014, **82**, 1205–1208.
3 European Commission, Brain research, **https://ec.europa.eu/info/research-and-innovation/research-area/health-research-and-innovation/brain-research_en**, (accessed 22 July 2021).
4 K. Ndyabawe and W. S. Kisaalita, *Drug Discovery Today*, 2019, **24**, 1725–1730.
5 T. Cameron, T. Bennet, E. M. Rowe, M. Anwer, C. L. Wellington and K. C. Cheung, *Micromachines*, 2021, **12**(4), 441.
6 Y. Zhao, U. Demirci, Y. Chen and P. Chen, *Lab Chip*, 2020, **20**, 1531–1543.
7 V. K. Gribkoff and L. K. Kaczmarek, *Neuropharmacology*, 2017, **120**, 11–19.
8 A. M. Taylor, S. W. Rhee, C. H. Tu, D. H. Cribbs, C. W. Cotman and N. L. Jeon, *Langmuir*, 2003, **19**, 1551–1556.
9 P. M. Holloway, S. Willaime-Morawek, R. Siow, M. Barber, R. M. Owens, A. D. Sharma, W. Rowan, E. Hill and M. Zagnoni, *J. Neurosci. Res.*, 2021, **99**, 1276–1307.
10 E. Neto, L. Leitão, D. M. Sousa, C. J. Alves, I. S. Alencastre, P. Aguiar and M. Lamghari, *J. Neurosci.*, 2016, **36**, 11573–11584.
11 S. Hosmane, M. A. Tegenge, L. Rajbhandari, P. Uapinyoying, N. Ganesh Kumar, N. Thakor and A. Venkatesan, *J. Neurosci.*, 2012, **32**, 7745–7757.
12 M. Ristola, L. Sukki, M. M. Azevedo, A. I. Seixas, J. B. Relvas, S. Narkilahti and P. Kallio, *J. Micromech. Microeng.*, 2019, **29**, 065009.
13 A. Ionescu, E. E. Zahavi, T. Gradus, K. Ben-Yaakov and E. Perlson, *Eur. J. Cell Biol.*, 2016, **95**, 69–88.
14 K. A. Southam, A. E. King, C. A. Blizzard, G. H. McCormack and T. C. Dickson, *J. Neurosci. Methods*, 2013, **218**, 164–169.
15 K. Sakai, K. Shimba, K. Ishizuka, Z. Yang, K. Oiwa, A. Takeuchi, K. Kotani and Y. Jimbo, *Biochem. Biophys. Res. Commun.*, 2017, **494**, 138–143.
16 S. Dauth, B. M. Maoz, S. P. Sheehy, M. A. Hemphill, T. Murty, M. K. Macedonia, A. M. Greer, B. Budnik and K. K. Parker, *J. Neurophysiol.*, 2017, **117**, 1320–1341.
17 M. Kamudzandu, M. Köse-Dunn, M. G. Evans, R. A. Fricker and P. Roach, *Biomed. Phys. Eng. Express*, 2019, **5**, 045016.
18 T. T. Kanagasabapathi, M. Franco, R. A. Barone, S. Martinoia, W. J. Wadman and M. M. J. Decré, *J. Neurosci. Methods*, 2013, **214**, 1–8.
19 X. Zhao, X.-Q. Chen, E. Han, Y. Hu, P. Paik, Z. Ding, J. Overman, A. L. Lau, S. H. Shahmoradian, W. Chiu, L. M. Thompson, C. Wu and W. C. Mobley, *Proc. Natl. Acad. Sci. U. S. A.*, 2016, **113**, E5655–E5664.
20 D. Kilinc, J. M. Peyrin, V. Soubeyre, S. Magnifico, L. Saias, J. L. Viovy and B. Brugg, *Neurotoxic. Res.*, 2011, **19**, 149–161.
21 Z. Tong, M. Segura-Feliu, O. Seira, A. Homs-Corbera, J. A. Del Río and J. Samitier, *RSC Adv.*, 2015, **5**, 73457–73466.
22 N. R. Wevers, D. G. Kasi, T. Gray, K. J. Wilschut, B. Smith, R. van Vught, F. Shimizu, Y. Sano, T. Kanda, G. Marsh, S. J. Trietsch, P. Vulto, H. L. Lanz and B. Obermeier, *Fluids Barriers CNS*, 2018, **15**, 23.
23 M. Campisi, Y. Shin, T. Osaki, C. Hajal, V. Chiono and R. D. Kamm, *Biomaterials*, 2018, **180**, 117–129.
24 N. R. Wevers, R. van Vught, K. J. Wilschut, A. Nicolas, C. Chiang, H. L. Lanz, S. J. Trietsch, J. Joore and P. Vulto, *Sci. Rep.*, 2016, **6**, 38856.
25 X. Chen, C. Liu, L. Muok, C. Zeng and Y. Li, *Cell*, 2021, **10**, 3183.
26 G. D. Vatine, R. Barrile, M. J. Workman, S. Sances, B. K. Barriga, M. Rahnama, S. Barthakur, M. Kasendra, C. Lucchesi, J. Kerns, N. Wen, W. R. Spivia, Z. Chen, J. Van Eyk and C. N. Svendsen, *Cell Stem Cell*, 2019, **24**, 995–1005.e6.
27 H. H. T. Middelkamp, A. H. A. Verboven, A. G. D. S. Vivas, C. Schoenmaker, T. M. K. Gunnewiek, R. Passier, C. A. Albers, P. A. C. 't Hoen, N. N. Kasri and A. D. van der Meer, *Sci. Rep.*, 2021, **11**, 2281.
28 S. Dekker, W. Buesink, M. Blom, M. Alessio, N. Verplanck, M. Hihoud, C. Dehan, W. César, A. Le Nel, A. van den Berg and M. Odijk, *Sens. Actuators, B*, 2018, **272**, 468–478.
29 K. Vittayarukskul and A. P. Lee, *J. Micromech. Microeng.*, 2017, **27**, 035004.
30 C. E. Owens and A. J. Hart, *Lab Chip*, 2018, **18**, 890–901.
31 R. Hernández Vera, P. O'Callaghan, N. Fatsis-Kavalopoulos and J. Kreuger, *Sci. Rep.*, 2019, **9**, 11321.
32 W. Shang, C. Y. Chen, K. Lo, G. F. Payne and W. E. Bentley, *Sens. Actuators, B*, 2019, **295**, 30–39.
33 X. Xie, S. Maharjan, S. Liu, Y. S. Zhang and C. Livermore, *Micromachines*, 2019, **11**, 2.
34 M. Rhee and M. A. Burns, *Lab Chip*, 2008, **8**, 1365–1373.
35 S. M. Langelier, E. Livak-Dahl, A. J. Manzo, B. N. Johnson, N. G. Walter and M. A. Burns, *Lab Chip*, 2011, **11**, 1679–1687.
36 P. M. Holloway, G. I. Hallinan, M. Hegde, S. I. R. Lane, K. Deinhardt and J. West, *Lab Chip*, 2019, **19**, 1484–1489.
37 C. MacKerron, G. Robertson, M. Zagnoni and T. J. Bushell, *Sci. Rep.*, 2017, **7**, 15692.
38 G. Robertson, T. J. Bushell and M. Zagnoni, *Integr. Biol.*, 2014, **6**, 636–644.
39 U. Ganguly, S. Singh, S. Pal, S. Prasad, B. K. Agrawal, R. V. Saini and S. Chakrabarti, *Front. Aging Neurosci.*, 2021, **13**, 365.
40 Y. Chen, K. S. Dolt, M. Kriek, T. Baker, P. Downey, N. J. Drummond, M. A. Canham, A. Natalwala, S. Rosser and T. Kunath, *Eur. J. Neurosci.*, 2019, **49**, 510–524.
41 L. A. Volpicelli-Daley, K. C. Luk, T. P. Patel, S. A. Tanik, D. M. Riddle, A. Stieber, D. F. Meaney, J. Q. Trojanowski and V. M. Y. Lee, *Neuron*, 2011, **72**, 57.

42 P. S. Mangan and J. Kapur, *J. Neurophysiol.*, 2004, **91**, 946–957.
43 S. E. Johnson, J. L. Hudson and J. Kapur, *J. Neurophysiol.*, 2015, **113**, 2461–2470.
44 M. Mele, R. Vieira, B. Correia, P. De Luca, F. V. Duarte, P. S. Pinheiro and C. B. Duarte, *Sci. Rep.*, 2021, **11**, 11374.
45 M. Serra, I. Pereiro, A. Yamada, J.-L. Viovy, S. Descroix and D. Ferraro, *Lab Chip*, 2017, **17**, 629–634.
46 D. Figura and J. Bartel, *ECS Trans.*, 2010, **25**, 29–35.
47 D. Johnson, J. Goettert, V. Singh and D. Yemane, *TechConnect Briefs*, 2012, **2**, 404–407.
48 J. J. K. Kim, H. Al Thuwaini and M. Almuslem, *Micro and Nano Systems Letters*, 2018, **6**, 14.
49 D. Sticker, M. Rothbauer, S. Lechner, M. T. Hehenberger and P. Ertl, *Lab Chip*, 2015, **15**, 4542–4554.
50 A. Bastiaens, J.-P. Frimat, T. Van Nunen and R. Luttge, *J. Vac. Sci. Technol., B*, 2019, **37**, 61802.
51 K. J. Pratt, S. K. Williams and B. E. Jarrell, *J. Biomed. Mater. Res.*, 1989, **23**, 1131–1147.
52 M. J. Lerman, J. Lembong, S. Muramoto, G. Gillen and J. P. Fisher, *Tissue Eng., Part B*, 2018, **24**, 359–372.
53 A. M. Taylor, M. Blurton-Jones, S. W. Rhee, D. H. Cribbs, C. W. Cotman and N. L. Jeon, *Nat. Methods*, 2005, **2**, 599–605.
54 P. M. Holloway, G. I. Hallinan, M. Hegde, S. I. R. Lane, K. Deinhardt and J. West, *Lab Chip*, 2019, **19**, 1484–1489.
55 A. Gladkov, Y. Pigareva, D. Kutyina, V. Kolpakov, A. Bukatin, I. Mukhina, V. Kazantsev and A. Pimashkin, *Sci. Rep.*, 2017, **7**, 1–14.
56 M. F. Duffy, T. J. Collier, J. R. Patterson, C. J. Kemp, D. L. Fischer, A. C. Stoll and C. E. Sortwell, *Front. Neurosci.*, 2018, **12**, 621.
57 K. C. Luk, C. Song, P. O'Brien, A. Stieber, J. R. Branch, K. R. Brunden, J. Q. Trojanowski and V. M. Y. Lee, *Proc. Natl. Acad. Sci. U. S. A.*, 2009, **106**, 20051–20056.
58 S. Gribaudo, P. Tixador, L. Bousset, A. Fenyi, P. Lino, R. Melki, J. M. Peyrin and A. L. Perrier, *Stem Cell Rep.*, 2019, **12**, 230–244.
59 Y. Shin, S. H. Choi, E. Kim, E. Bylykbashi, J. A. Kim, S. Chung, D. Y. Kim, R. D. Kamm and R. E. Tanzi, *Adv. Sci.*, 2019, **6**, 1900962.
60 J. H. Sung, Y. I. Wang, N. N. Sriram, M. Jackson, C. Long, J. J. Hickman and M. L. Shuler, *Anal. Chem.*, 2019, **91**, 330.
61 J. H. Lee, I. H. Lee, Y. J. Choe, S. Kang, H. Y. Kim, W. P. Gai, J. S. Hahn and S. R. Paik, *Biochem. J.*, 2009, **418**, 311–323.
62 M. Fayyad, N. K. Majbour, N. N. Vaikath, D. Erskine, H. El-Tarawneh, I. P. Sudhakaran, H. Abdesselem and O. M. A. El-Agnaf, *Neurosci. Lett.*, 2020, **725**, 134899.